PNAS
www.pnas.org

Supplementary Information for

Three-dimensional label-free visualization and quantification of polyhydroxyalkanoates in individual bacteria cell in its native state

So Young Choi, Jeonghun Oh, JaeHwang Jung, YoungKeun Park, and Sang Yup Lee

To whom correspondence may be addressed.
YoungKeun Park, Sang Yup Lee
Email: yk.park@kaist.ac.kr, leesy@kaist.ac.kr

This PDF file includes:

Other supplementary materials for this manuscript include the following:

SI Appendix Materials and Methods

Bacterial Strain and Cultivation. All bacterial strains and plasmids used in this study are listed in *SI Appendix,* Table S1. Poly(3-hydroxybutyrate) [PHB] producing strains, *C. necator* H16 and recombinant *E. coli* XL1-Blue (Stratagene Cloning Systems, La Jolla, CA, USA) harboring pCnCAB (1), were used in this study. The plasmid pCnCAB, which expresses *C. necator phaCAB* genes under the *C. necator* promoter of the *phaCAB* operon, has been previously described (1). The cells were routinely grown in Luria-Bertani (LB) broth (10 g/L tryptone, 5 g/L yeast extract, and 10 g/L NaCl) or on LB agar plate (LB supplemented with 1.5% (w/v) agar) supplemented with 50 μg/mL of ampicillin when necessary. For PHB production, *C. necator* and recombinant *E. coli* strains were seeded in 5 mL of LB broth, contained in 25 mL test-tubes, and cultured at 30°C with shaking, at 200 rpm. The *C. necator* seed culture was used to inoculate 100 mL of LB broth, contained in a 250 mL flask, and incubated at 30°C with shaking at 200 rpm. After a 12–18 h culture period, the cells were harvested by centrifugation and transferred to a fresh, nitrogen-limiting, chemically defined medium (6.67 g/L KH_2PO_4, 4 g/L Na_2HPO_4, 0.8 g/L citric acid, 0.8 g/L $MgSO_4$, and 5 mL/L trace metal solution), supplemented with 20 g/L fructose and incubated at 30°C with shaking at 200 rpm. The trace metal solution contains 10 g $FeSO_4 \cdot 7H_2O$, 2 g $CaCl_2$, 2.2 g $ZnSO_4 \cdot 7H_2O$, 0.5 g $MnSO_4 \cdot 4H_2O$, 1 g $CuSO_4 \cdot 5H_2O$, 0.1 g $(NH_4)_6Mo_7O_{24} \cdot 4H_2O$, and 0.02 g $Na_2B_4O_7 \cdot 10H_2O$, per liter of 0.5 M HCl. For poly(3HB-*co*-3HV) production, *C. necator* cells were cultivated in the same medium except that 5 g/L of levulinic acid was additionally added. The recombinant *E. coli* seed culture was used to inoculate 100 mL of LB broth with 20 g/L glucose, contained in a 250 mL flask, and incubated at 30°C with shaking at 200 rpm. All other recombinant *E. coli* strains including *phaP1* or *phaM*-expressing strains and poly(3HB-*co*-LA) producing strain and recombinant *K. pneumoniae* cells were cultured in the same manner.

For MCL-PHA production, *P. putida* KT2440 cells were cultured in the same way as the *E. coli,* except that sodium octanoate was supplemented to 3.3 g/L as a carbon source. For poly(3HB-*co*-LA) production, recombinant *E. coli* XL1-Blue harboring pPs619C1400Pct532-CnAB was used. The plasmid pPs619C1400Pct532-CnAB expresses engineered *Pseudomonas* sp. MBEL 6-19 *phaC* (*phaC1400*; E130D, S325T, S477R, and Q481M), engineered *Clostridium propionicum pct* (*pct532*; A243T and silent mutation of A1200G), and *C. necator phaAB* genes. To produce PHB, the recombinant *K. pneumoniae* harboring pKM312CnCAB which expresses *C. necator phaCAB* genes under *tac* promoter has been constructed. The recombinant *E. coli* strains additionally express *C. necator phaP1* or *phaM* have been constructed by the transformation of *E. coli* XL1-Blue with plasmids pCnP1CAB or pCnMCAB, respectively.

To visualize the PHA granule using green fluorescent protein (GFP) as a reporter protein, sfGFP (super folder GFP) was fused to the N-terminus of the PHA synthase (PhaC) with a GGGGSG linker, resulting in the sfGFP-PhaC fusion protein. Plasmid pCn-sfGFP-L-CAB expressing the *sfgfp-phaC* and *phaAB* genes was constructed by cloning the *sfgfp-phaC* gene to the plasmid pCnCAB instead of the *phaC* gene. For comparison, the two *sfgfp*-expression plasmids were also constructed. The one is pCn-sfGFP-CAB which expresses *sfgfp* and *phaC* genes individually with *phaAB* genes. The other is pCn-sfGFP-AB which expresses *sfgfp* and *phaAB* genes. The *E. coli* XL1-Blue strains harboring each of these plasmids were cultivated under the same condition used for the other *E. coli* cells mentioned above.

Gas Chromatography Analysis. The PHA contents were determined by gas chromatography (GC) analysis (2–4). The cultured cells were harvested by centrifugation at 4,000 × g for 15 min, washed twice with distilled water, and dried overnight at 70°C. The dried cell pellet was subjected to methanolysis, with benzoic acid as an internal standard, in the presence of 15% sulfuric acid. The resulting methyl esters of PHA monomers (3-hydroxybutyrate, 3-hydroxyvalerate, lactate, 3-hydroxyhexanoate, 3-hydroxyoctanoate, and 3-hydroxydecanoate) were analyzed by GC according to the previous study (4). GC analysis was performed by injecting 1 μL of a sample into Agilent 6890N GC system (Agilent Technologies, Palo Alto, CA, USA) equipped with Agilent 7683 automatic injector, flame ionization detector, and fused silica capillary column (AT™-Wax, 30 m, ID 0.53 mm, film thickness 1.20 μm, Alltech, Deerfield, IL, USA). Nitrogen was used as a carrier gas. Using GC analysis, PHA content (%, w/w) was calculated as a percentage of PHA concentration to DCW concentration.

Sample Preparation for Optical Imaging. For single-cell imaging, the culture broth was diluted, with the same medium, to obtain a cell density of approximately 10^6 cells/mL. For fluorescence imaging, Nile Red (19123, Sigma-Aldrich Inc., St. Louis, MO, USA) solution in dimethyl sulfoxide (10 mg/mL) was added to the diluted bacterial solution such that the final concentration of Nile Red in the solution was 5 μg/mL. Thereafter, the solution was incubated for 3 min at room temperature (25°C) in dark. Subsequently, 18 μL of the sample solution was transferred onto a TomoDish (Tomocube Inc., Daejeon, Republic of Korea)—a specially designed dish with a glass window at the center of the bottom face—and a coverslip was gently put on the top of the sample solution to seal it. In the case of real-time analyses, the dish was kept in a heated place at 30°C during measurements in order to keep the sample viable.

Optical Diffraction Tomography. The sample on the glass coverslip is sequentially illuminated by plane waves at 71 illumination angles (*SI Appendix*, Fig. S1). The light diffracted from the sample, at each illumination angle, is recorded in spatially modulated holograms using a quantitative phase imaging technique (5, 6) (*SI Appendix*, Fig. S1). Corresponding 2D optical field information—amplitude and phase of the diffracted light—are retrieved from each hologram via the field retrieval algorithm (7, 8) (*SI Appendix*, Fig. S1). 3D RI distribution of the sample is reconstructed from multiple 2D optical fields measured, based on the Fourier diffraction theorem (9, 10). The missing information, due to limited illumination and detection angles of the optical lenses, is filled in by exploiting an iterative non-negative constraint method (11). The 3D visualization of RI distribution is rendered using commercial software (TomoStudio™, Tomocube Inc., Daejeon, Republic of Korea).

The ODT system is constructed based on Mach-Zehnder interferometry (*SI Appendix*, Fig. S2). We exploited a commercial ODT system (HT-2H, Tomocube Inc., Republic of Korea). The beam from a coherent light source (wavelength of 532 nm) was split into two pathways, a sample beam path, and a reference beam path. A digital micromirror device, located at the conjugate plane of the sample, allows for rapid control of incident angles of the illumination plane waves by displaying the grating patterns at desired periods and directions. Unwanted diffraction orders of the grating patterns were minimized employing the technique based on temporal multiplexing (12, 13). The plane wave at the controlled angle illuminated a sample via a high numerical aperture (NA) objective lens (NA = 1.2, water immersion, UPLSAPO 60XW, Olympus Inc., Tokyo, Japan) and the diffracted wave from the sample was collected via the high NA objective lens (NA = 1.2, water immersion, UPLSAPO 60XW, Olympus Inc., Tokyo, Japan). The maximum incident angle corresponds to approximately 45° in a sample medium. The sample beam and the reference beam combined through a beam splitter and produced spatially modulated holograms in a camera plane. The spatially modulated holograms were recorded by a CMOS camera (FL3-U3-13Y3M-C, Point Grey Research Inc., Vancouver, Canada). The total acquisition time for 49 holograms was approximately 400 ms (8 ms per hologram). The theoretically calculated lateral and axial resolutions of the ODT system were 110 nm and 360 nm, respectively (14).

Wide-Field Fluorescence Analysis. The PHA granules stained with Nile Red were analyzed by the ODT system equipped with a wide-field fluorescence microscopic module. A diode-pumped solid-state laser (532 nm, Samba™, Cobolt Inc., Solna, Sweden) was used as the excitation source for Nile Red. After the ODT measurements of a sample were made, a notch filter with the central stopband wavelength of 532 nm (FL532-1, Thorlabs Inc., Newton, NJ, USA) was manually inserted in front of the camera to block the excitation light from the laser. Then, wide-field fluorescence images of the cells were captured.

The PHA granules labeled with sfGFP were analyzed by the same ODT system. After the bacterial cells were reconstructed into the 3D RI distributions, a LED light source (470 nm) excited the cells to detect the green fluorescence signal with a bandpass filter of 500–550 nm for emission. The acquired fluorescence images were reproduced using computational deconvolution for an improved resolution and higher signal-to-noise ratio.

Quantification of Cell Parameters. Variations between the cells, cellular volume, dry cell weight (DCW), PHA weight, and PHA ratio of individual cells were quantified from the reconstructed 3D RI

distributions. Cell volume was determined by the cell boundary identified in the RI distribution. The density of PHA granules is calculated from the RI value by supposing that PHA density is linearly proportional to PHA RI. Although there are various mathematical models that show a relationship between density and RI of material, including Lorentz-Lorenz, Newton-Drude, and Gladstone-Dale formulas, they allow for an approximately linear relation between density and RI. Since there is no direct report on the exact relationship between the density and the RI of PHAs, we constructed a linear equation model. We found that the RI values of the PHA were mostly distributed between 1.390 and 1.410, and presumed that PHA density is 1.10 g/mL at a RI of 1.390 and 1.20 g/mL at a RI of 1.410 with the linear relation because the density of amorphous PHA is approximately 1.15 g/mL (15). The coefficient for the linear relation is derived from glass (16, 17). DCW is calculated as the sum of weights of PHA and non-PHA. The weight of PHAs accumulated in the cells is obtained from the volume (RI > 1.390) and density of the granules. To calculate the non-PHA weight of the cell, we utilized the linear relationship between RI and solution concentration (18):

$$n_s = n_m + \sum_i \alpha_i C_i \tag{1}$$

where n_s, n_m, α_i, and C_i indicate RI of the solution, RI of the medium, RI increment of i^{th} component, and concentration of i^{th} component. Supposing the PHA-excluded cytoplasm is an aqueous solution, the concentration of non-PHA components could be obtained from the reconstructed RI distribution using **Eq. (1)**. Since most biological components, including proteins, nucleic acids, salts, and sugars, have comparable RI increment values (19–22), we used a constant RI increment value of 0.185 mL/g for biological components. Thereafter, the 3D distribution of the average concentration of non-PHA cellular components was obtained from 3D RI distribution (18, 23). Non-PHA weight was calculated by integrating the concentration over non-PHA volume. PHA ratio is defined as the ratio of PHA weight to DCW.

Polarity and Centrality Analyses. For easy manipulation of the digitized 3D RI distribution of the sample, we first aligned the long axis of the bacteria parallel to the x-axis by detecting the 3D orientation of the cells. Thereafter, the center of the cell is determined via ellipse fitting of the cell boundary in the *xy*-plane-projected image. The cell length, L_{cell}, is measured as the distance between two points produced by intersecting the cell boundary and a line along the *x*-axis passing through the cell center. We identified PHA regions by applying the RI threshold of 1.390 and the measured distance L_{PHA} between the identified pixel and the cell center along the *x*-axis. Thus, the polarity of each PHA pixel was calculated as

$$\frac{L_{\text{PHA}}}{L_{\text{cell}}/2} \ . \tag{2}$$

To calculate centrality, the sample was digitally sliced perpendicular to the longitudinal axis of the cell. For each slice, the cross-sectioned image of the cell was fitted into an ellipse. For a given PHA pixel, the distance from the center to the membrane, D_{mem}, was measured as the distance from the center to the fitted ellipse on the line connecting the center and the selected PHA pixel. The distance D_{PHA} was defined as the length between a PHA pixel and the center of the ellipse. Thus, the centrality of the PHA pixel is calculated as

$$\frac{D_{\text{mem}} - D_{\text{PHA}}}{D_{\text{mem}}} \ .$$

Mean PHA polarity and centrality of the cell are the averages of the polarity and centrality of every PHA pixel in the cell, respectively. Since the localization with too few voxels may lead to distorted results, we measured the localization for cells with statistically significant granule voxels (five or more).

SI Appendix Text S1

Different Techniques for Observation of *in Vivo* PHA Granules. Previous studies on investigating *in vivo* PHA granules have been performed by using fluorescence microscopy (24–26), TEM (27, 28), and electron cryotomography (29). These techniques have generally relied on the statistical analysis of multiple 2D snapshots of different fixed cells or short-time monitoring of the cells (24–29). For the TEM analysis, cells need to be fixed and sectioned, and thus the investigation of living cells is not possible. The fluorescence-based techniques require fluorescence labeling, such as fusion of GFP reporter protein to PHA synthase (that associates with the PHA granules) or Nile Red staining of PHAs. Indirect imaging with the use of reporter protein cannot show the native state of PHAs or cells. Moreover, invasive exogenous dyes can affect the physiology and viability of the cells. In addition, there is a possibility that each sample might be stained to a different extent, thereby hindering accurate imaging analysis. On the other hand, ODT analysis is based on the measurement of RI distributions. RI is an intrinsic optical property of a substance, and thus visualization of 3D structures of a sample is available via RI contrast without exogenous labeling or destructive preparation processes. It allows the real-time quantitative analysis of living cells in the culture medium, as demonstrated by showing the dynamics of living cells and *in vivo* PHB granules over 8 h in this study. In addition, we used fluorescence imaging to compare the results obtained with RI distribution. Also, other complementary techniques such as the ones based on intrinsic properties, like polarization (30) and spectral dispersion (31), can be easily employed in holographic measurements. Thus, it is expected that further studies will provide a clearer understanding of the *in vivo* accumulation of PHA and other important biological behaviors.

SI Appendix Text S2

Quantification of PHB Content by Gas Chromatography Analysis. GC analysis is a routinely used method for determining PHA concentration and content. For comparison with the PHB content quantified by ODT analysis, GC analysis was performed (*SI Appendix*, Table S2). It should be noted that the PHB contents (and concentrations) obtained by GC analysis cannot be directly compared with those obtained with ODT analysis for the following reasons. For GC analysis, PHB in the dried cells is subjected to hydrolysis and methanolysis, converting 3-hydroxybutyrate (3HB) into methyl-3-hydroxybutyrate (ME-3HB), which is detected and measured by GC. In the sample preparation process, 3HB, 3HB oligomers, and low molecular weight PHB which exist as soluble and partially soluble in cells are also converted to ME-3HB, thus presenting differences between the two methods. As shown in *SI Appendix*, Table S2, the PHB contents obtained by GC analyses were higher than the PHB granule contents obtained by ODT analyses. The ODT analysis is uniquely advantageous as it allows monitoring of individual live cells without any labeling, which had not been possible before. The ODT analysis sets the specific criteria of refractive index (RI) for PHB granule based on the 3D visualization. Thus, it does not measure the soluble or partially soluble monomers or oligomers, allowing examination of only PHB granules, which is another advantage. Furthermore, ODT analysis takes much less time (a few minutes) than GC analysis (many hours including sample preparation and analysis).

SI Appendix Text S3

Fluorescence Microscopic Analysis. To further confirm the identified *in vivo* PHA granules from ODT analysis, we performed the fluorescence microscopy (FM) analysis for the PHA granules using green fluorescent protein (GFP) as a reporter protein. To label PHA granules with GFP, the sfGFP (super folder GFP) was fused to the N-terminus of the PHA synthase (PhaC), resulting in the sfGFP-PhaC fusion protein (*SI Appendix*, *Materials and Methods* and Table S1).

When the cells of recombinant *E. coli* expressing s*fgfp-phaC* and *phaAB* genes were concurrently subjected to ODT and FM, the green fluorescence from the FM corresponded well to the PHB granule, which is the region of RI > 1.39 from the ODT (*SI Appendix*, Fig. S5*A*). The relatively high intensity of the fluorescence was detected at the granule boundary region, indicating the sfGFP-PhaC fusion protein was localized at the granule surface region.

For comparison, we also examined the control *E. coli* expressing *sfgfp* without labeling of PHA granules under PHB-producing (co-expressing *phaCAB* genes) or non-PHB-producing (co-expressing *phaAB* genes only) conditions. In the case of the PHB-producing *E. coli,* as expected,

the FM showed that the green fluorescence was detected only at the cytoplasmic space, while the region with the PHB granules having RI > 1.39 by the ODT analysis did not show any fluorescence (*SI Appendix*, Fig. S5*B*). We also observed that the green fluorescence was not detected in some of the RI regions of 1.37–1.39 (near to 1.39). It can be inferred that as the RI value approaches 1.39, the region indicates more densely packed polymer chains to form the insoluble granules which become distinct from the cytoplasm. In the case of the other control *E. coli* strain (non-PHB-producing), the green fluorescence from the FM was shown throughout the cytoplasm, and the RI values via ODT were overall below 1.37 (*SI Appendix*, Fig. S5*C*).

In conclusion, through the analyses of ODT and FM (Nile-red stained granules shown in Fig. 1 and sfGFP-labeled granules described in this section), we provide detailed explanations on the *in vivo* PHA into two parts: (1) the region of RI > 1.39 corresponds to the PHA granules, and (2) the region of 1.37–1.39 corresponds to the relatively mobile surface region that includes the PHA polymeric chains which have not yet formed into granules and also the relatively mobile region near the surface of PHA granule.

SI Appendix Text S4

Quantification for Real-Time Analysis. The dynamic changes of cells and *in vivo* PHB granules shown in Movie S4 were quantitatively analyzed at the individual cell level (*SI Appendix*, Fig. S9). The cell ‘1’ generated two daughter cells, ‘1a’ and ‘1b’ at 100 min and the cell ‘1a’ generated two daughter cells, ‘1aa’ and ‘1ab’ at 200 min (*SI Appendix*, Fig. S9*A*). Combined with the cell division, the changes in cell volume, PHB content, and PHB granule polarity of the cells were clearly observed (*SI Appendix*, Fig. S9*B*). The PHB content of cell ‘1a’ was nearly 0% right after cell division at 100 min, since the accumulated PHB granules of cell ‘1’ were transferred to the cell ‘1b’, resulting in cell ‘1b’ harboring PHB with a PHB content of 50% (*SI Appendix*, Fig. S9*B*). This phenomenon was also observed for other cells including the cell ‘1aa’ with a PHB content of about 30% (200 min) when the cells ‘1a’ were dividing.

As shown in *SI Appendix*, Fig. S9*B*, the PHB content decreased at certain time points, e.g. cell ‘1b’ at 200–350 min. This decrease occurred when the increase in cell weight during cell elongation was greater than the increase in PHB granule weight. Similarly, the increase in polarity could be explained by cell elongation, when PHB granules remained at the poles (*SI Appendix*, Fig. S9*B*).

SI Appendix Figures

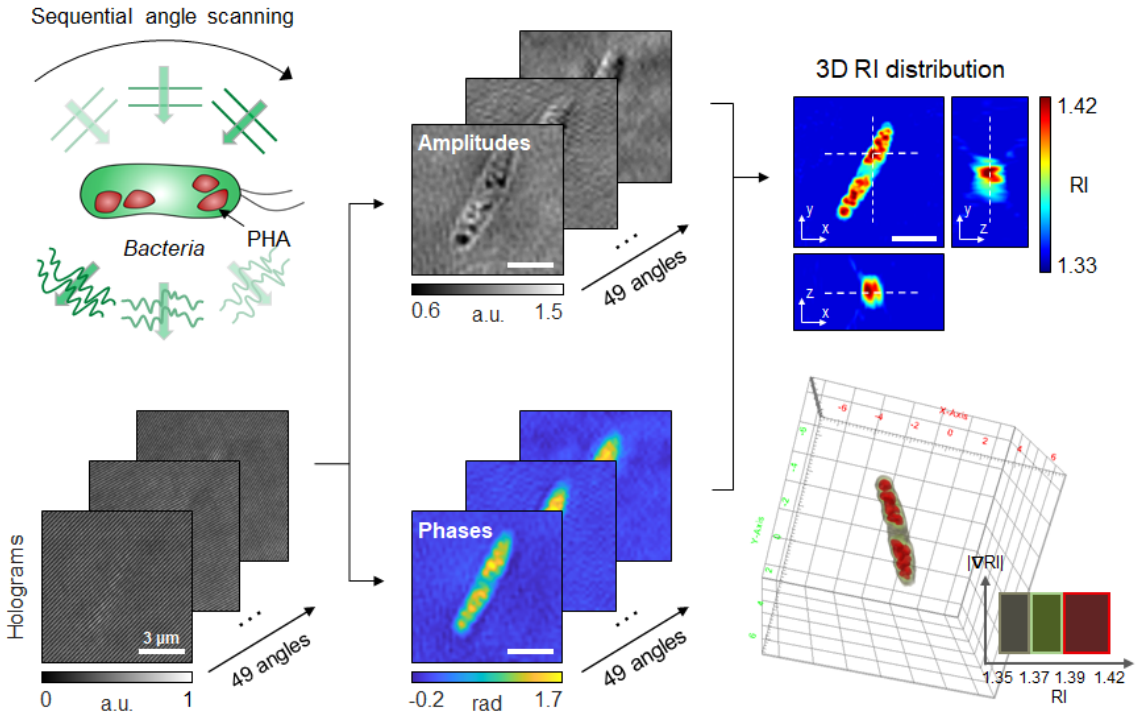

Fig. S1. Schematic process of optical diffraction tomography. A sample is illuminated at multiple sequential illumination angles (*Left, Top*). Raw holograms recorded at individual angles (*Left, Bottom*). Retrieved quantitative amplitude and phase information (*Middle*). Cross-sectional images of reconstructed 3D RI distribution and 3D rendering image of the sample (*Right*). In the 3D rendering image, one grid equals 2 μm.

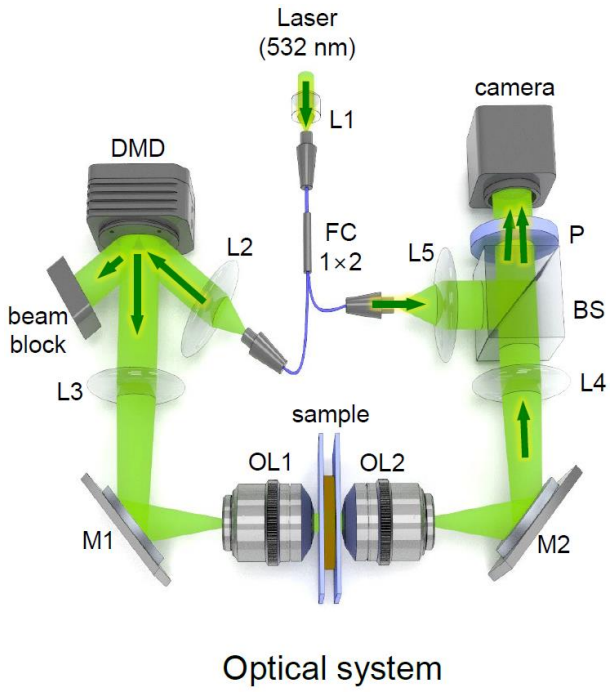

Fig. S2. Optical system for optical diffraction tomography (ODT). Individual holograms are recorded based on Mach-Zehnder interferometric microscopy. Incident angles are controlled via displaying appropriate binary patterns on DMD. L1-5: lens; M1-2: mirrors; OL1-2: objective lens; DMD: digital micromirror device; FC: fiber coupler; BS: beam splitter; P: polarizer.

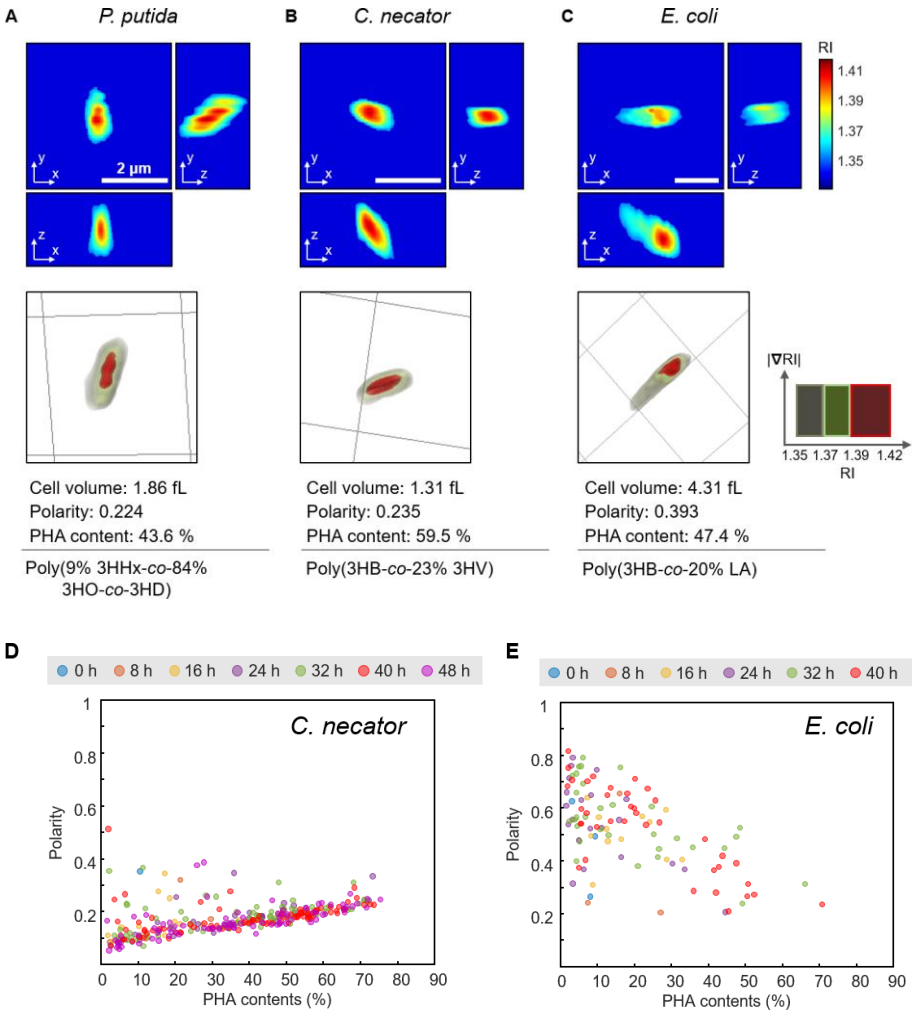

Fig. S3. Representative 3D RI distributions of bacterial cells and correlative analyses. (*A*) *P. putida* cell accumulating MCL-PHA at 20 h of cultivation. (*B*) *C. necator* cell accumulating poly(3HB-*co*-3HV) at 48 h of cultivation. (*C*) Recombinant *E. coli* cell accumulating poly(3HB-*co*-LA) at 40 h of cultivation. RI tomograms at selected x-y, y-z, and z-x planes (top) and 3D rendering images of the cells (bottom) are shown. The cell volume, polarity, and PHA content (%, w/w) quantified by ODT analyses are noted below the rendering images. The PHA compositions were obtained by GC analyses. In the 3D rendering images, one grid equals 5 μm. Scatter plots of polarity vs. PHA content for (*D*) *C. necator* cells accumulating poly(3HB-*co*-3HV) and (*E*) recombinant *E. coli* cells accumulating poly(3HB-*co*-LA).

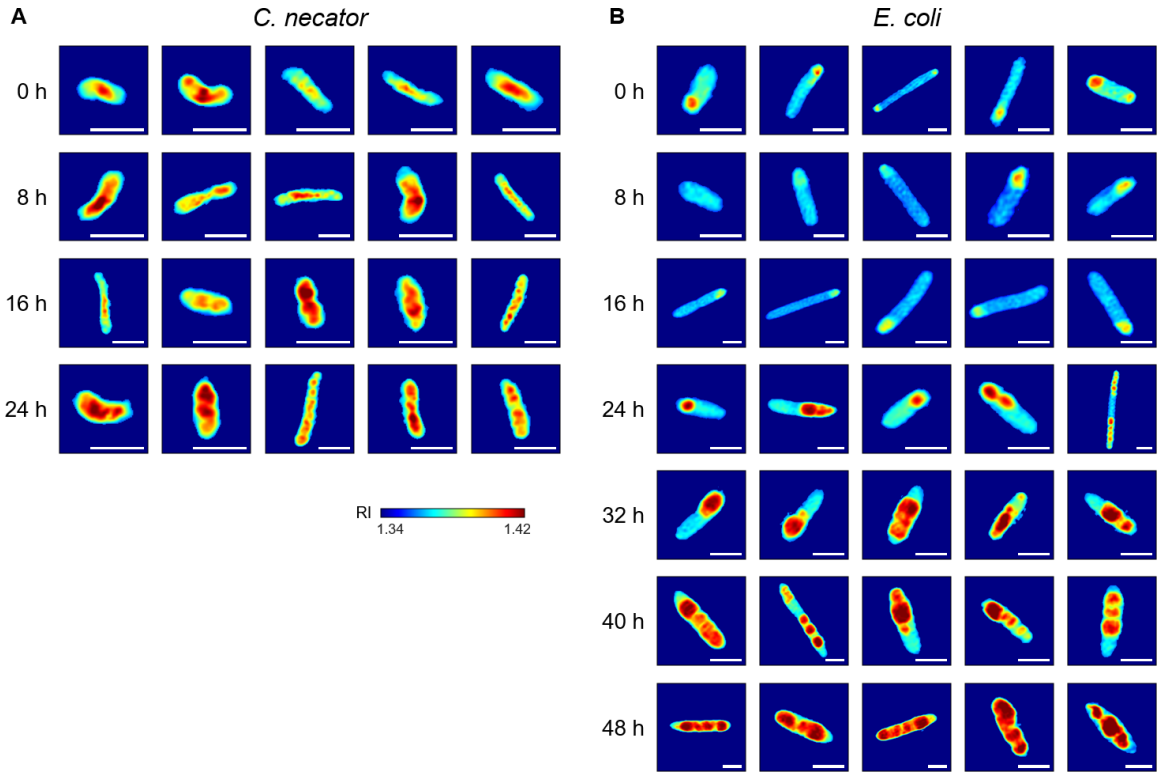

Fig. S4. RI projection images of (*A*) *C. necator* cells and (*B*) recombinant *E. coli* cells at different culture times. Scale bar, 2 μm.

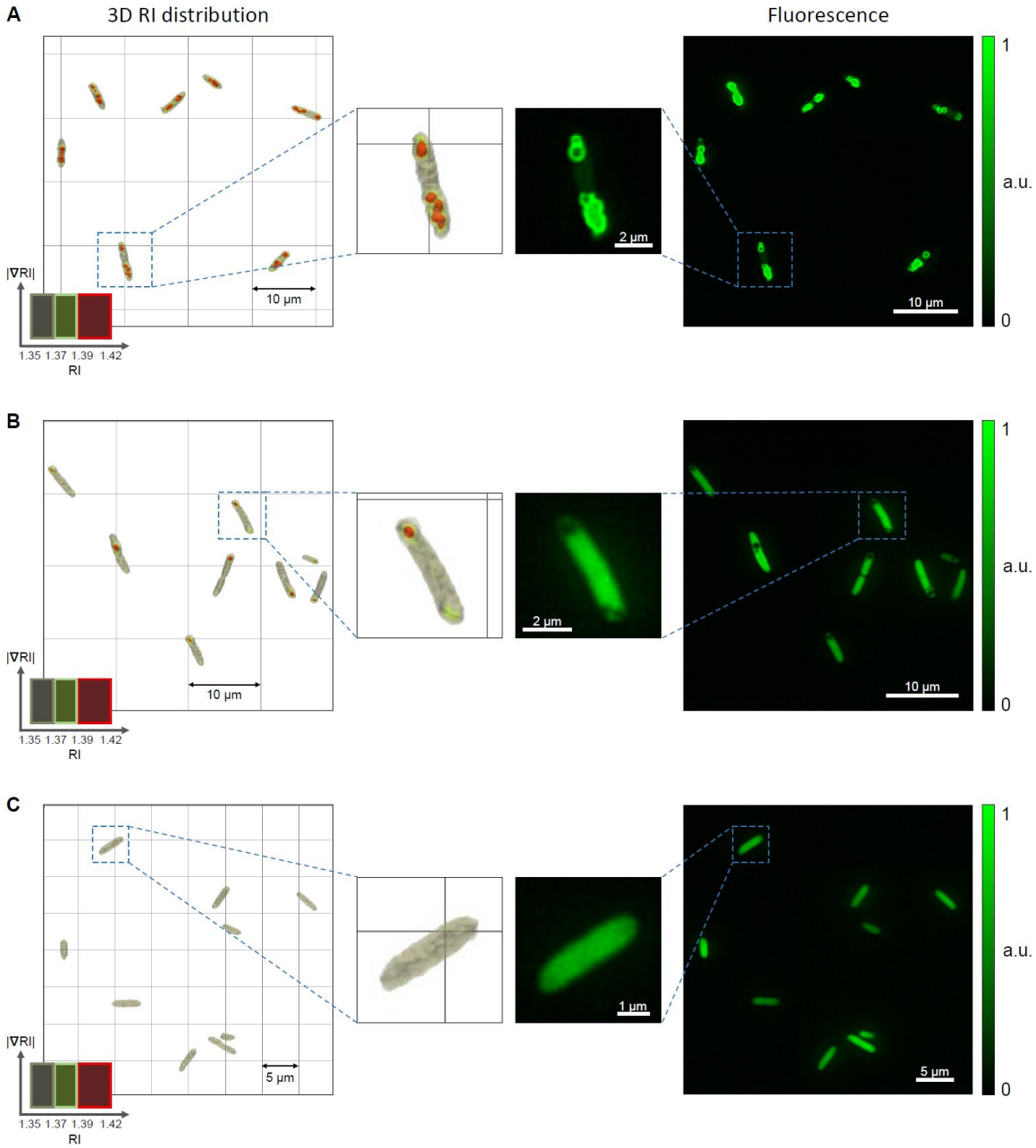

Fig. S5. The visualization of the 3D RI distribution and its correlative fluorescence image for the cells of (*A*) recombinant *E. coli* expressing *sfgfp-phaC* and *phaAB*, (*B*) recombinant *E. coli* expressing *sfgfp, phaC*, and *phaAB*, and (*C*) recombinant *E. coli* expressing *sfgfp* and *phaAB*.

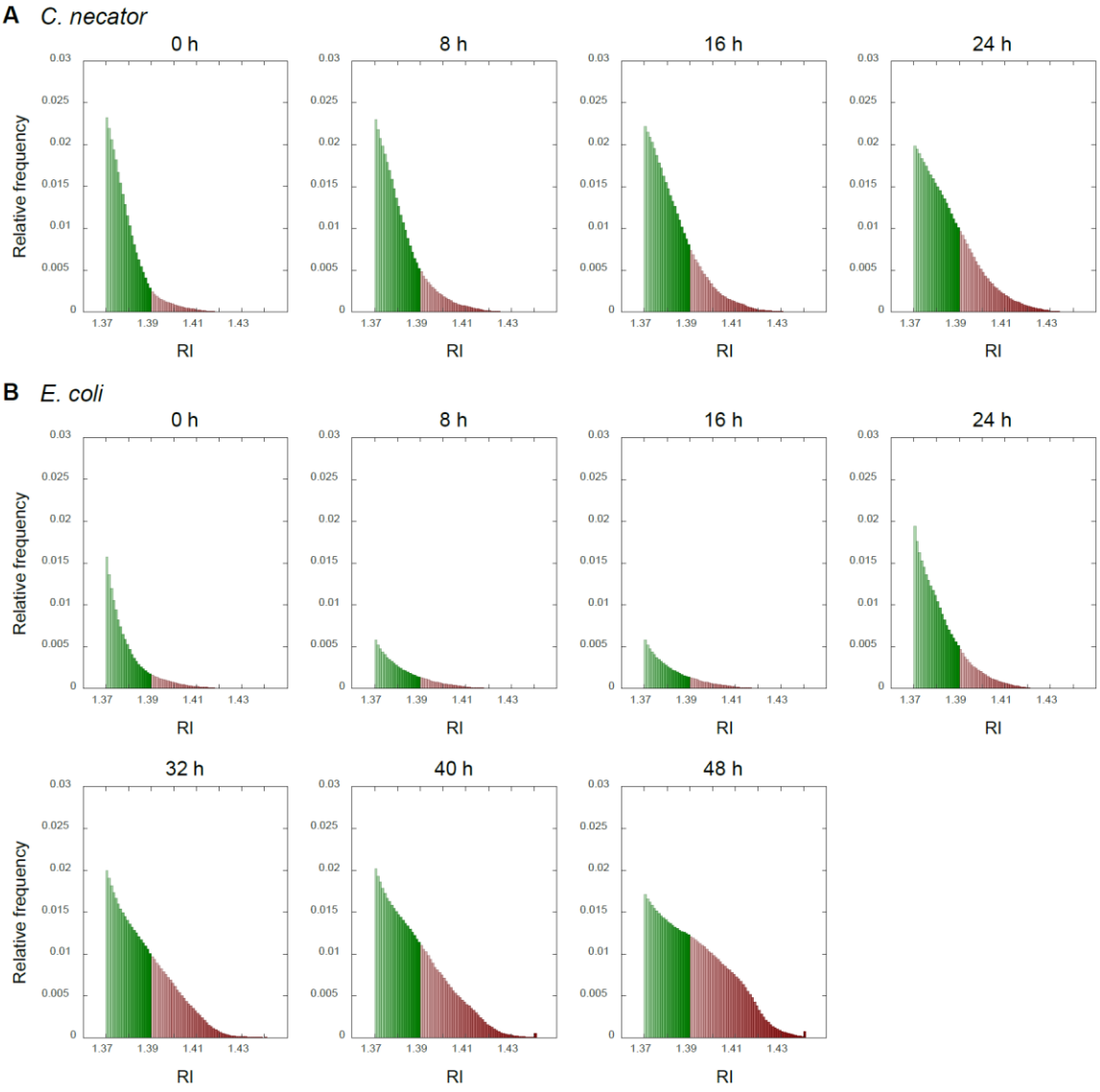

Fig. S6. RI distribution analysis. After evaluating the relative frequencies of the number of voxels in each cell corresponding to RI intervals for all the number of voxels inside the cell, the relative frequencies are averaged for all cells. The RI interval length is 0.001 from 1.37 to 1.44, and the RI intervals higher 1.44 are all combined. (*A*) *C. necator* cells for 0–24 h. *(B)* Recombinant *E. coli* cells for 0–48 h.

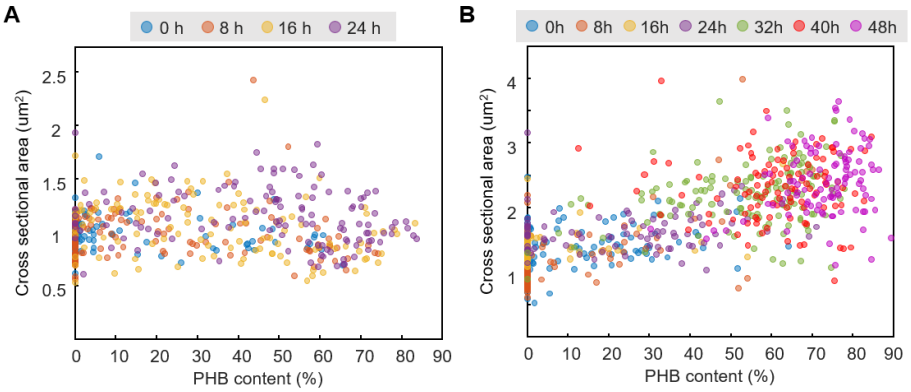

Fig. S7. Correlative analyses. (*A*, *B*) Scatter plots of cross sectional area of cell vs. PHB content for *C. necator* and recombinant *E. coli,* respectively.

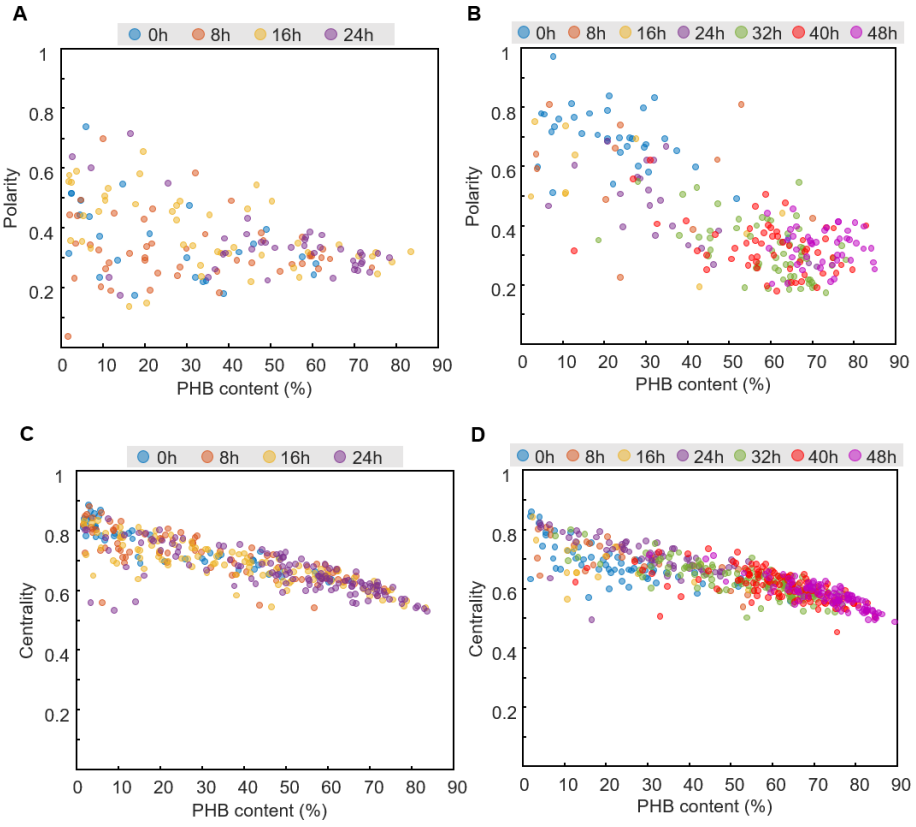

Fig. S8. Correlative analyses for localization. (*A*, *B*) Scatter plots of polarity vs. PHB content for *C. necator* and recombinant *E. coli,* respectively. Each plot covers only the cells which are longer than the average cell length. (*C*, *D*) Scatter plots of centrality vs. PHB content for *C. necator* and recombinant *E. coli,* respectively.

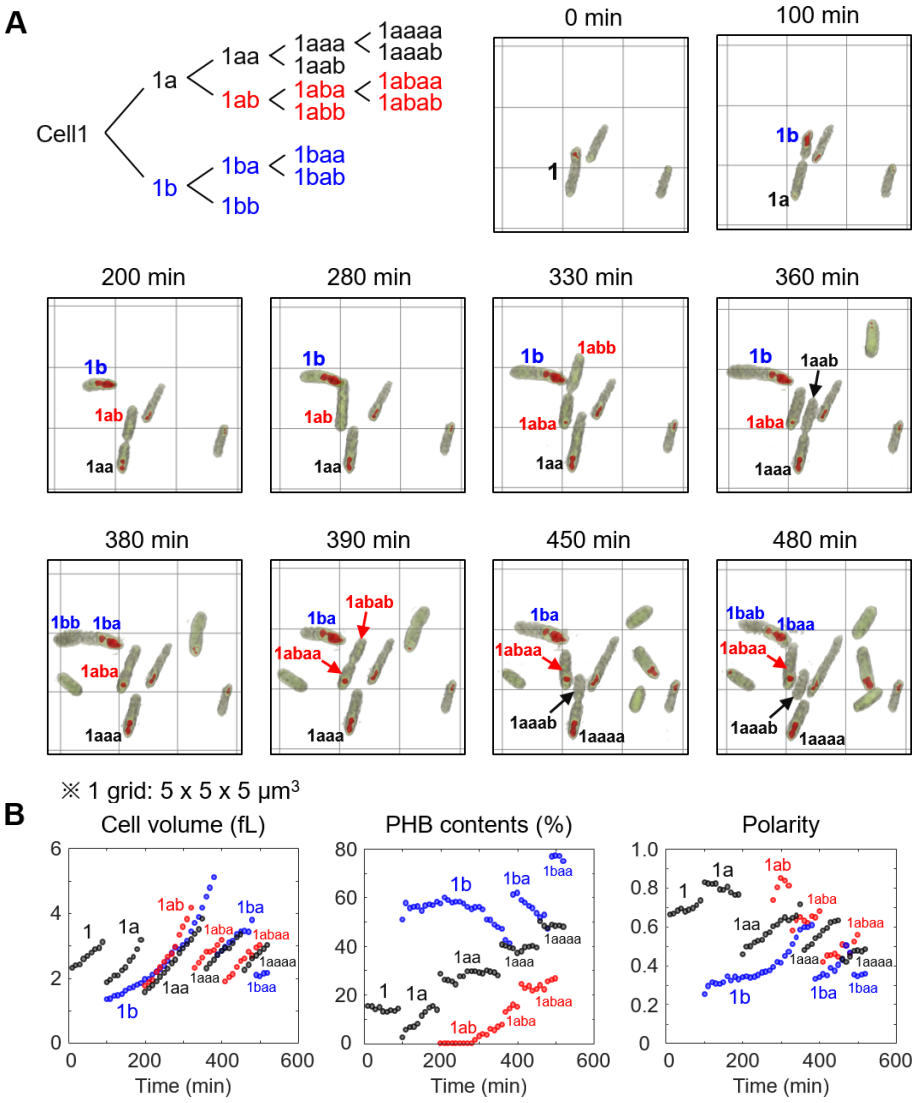

Fig. S9. Real-time investigation of recombinant *E. coli* cells for 520 min. (*A*) Schematic representation of cell division and 3D rendering images of the cells. The cell '1' divided into two daughter cells indicated as '1a' and '1b'. PHB granules are indicated in red. (*B*) Time profiles of cell volume, PHB content (%, w/w), and PHB granule polarity.

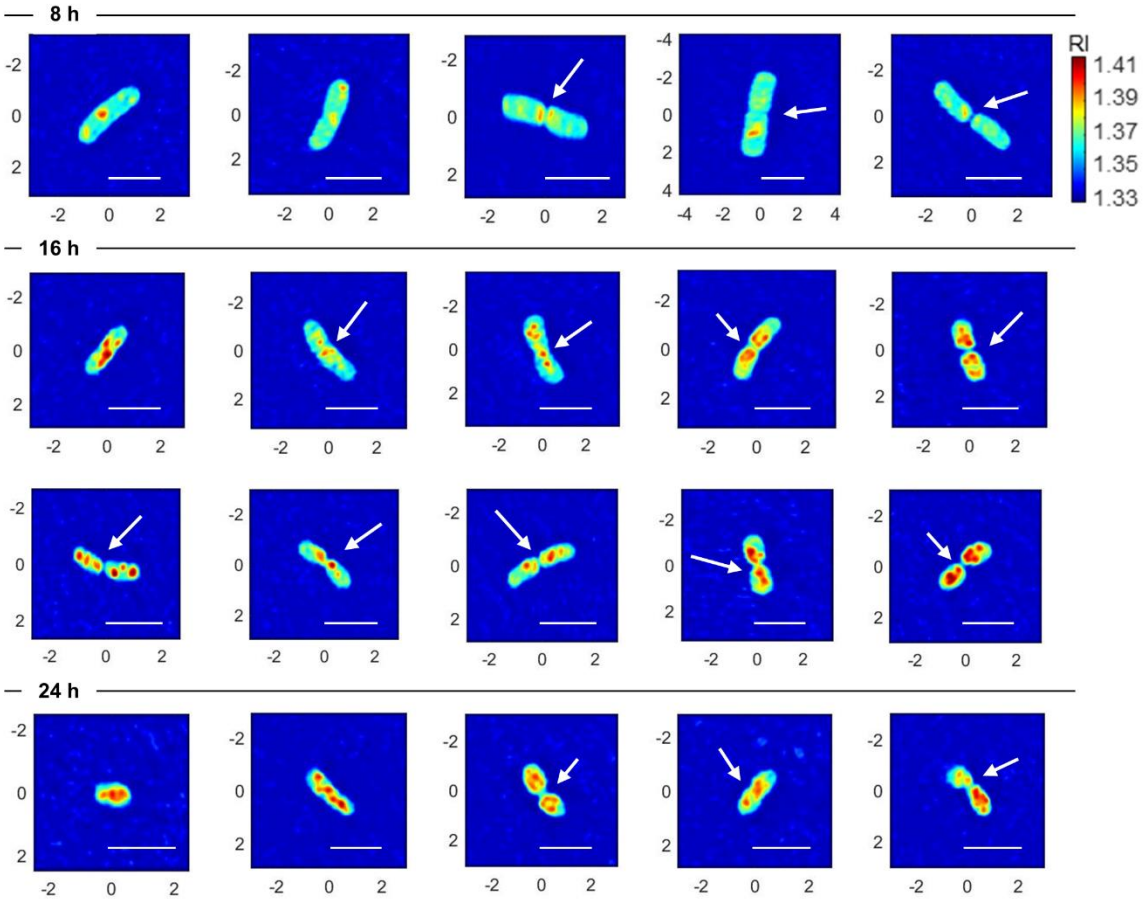

Fig. S10. 3D RI distributions of *C. necator* cells, which were cultivated in nitrogen-deficient medium for 8, 16, and 24 h, respectively. The arrows indicate expected cell division sites. Scale bar, 2 μm.

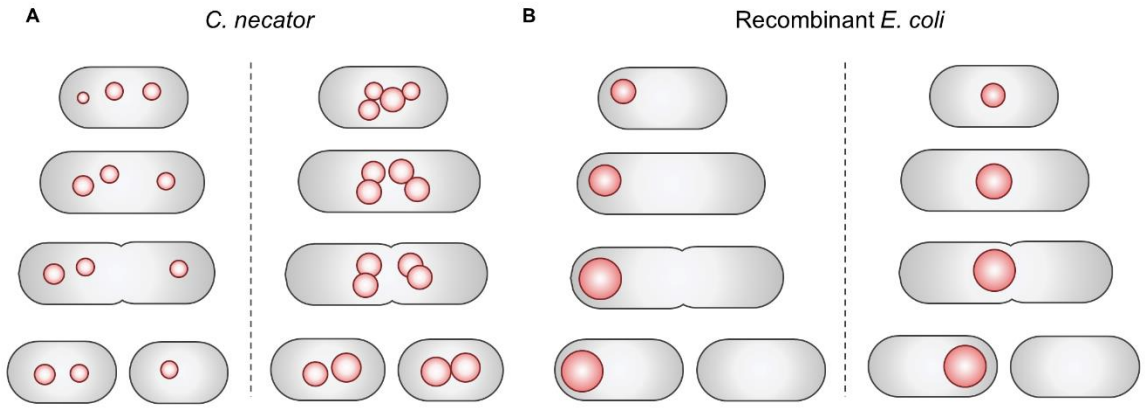

Fig. S11. Schematic representations for the PHB granule localization with cell division in (*A*) *C. necator* and (*B*) recombinant *E. coli* cells. PHB granules are indicated by red circles. Note that the localization pattern can be more complex since the volume of PHB granules can continually increase, in some cases, as much as volume of the cell body and a cell can have more than one PHB granules.

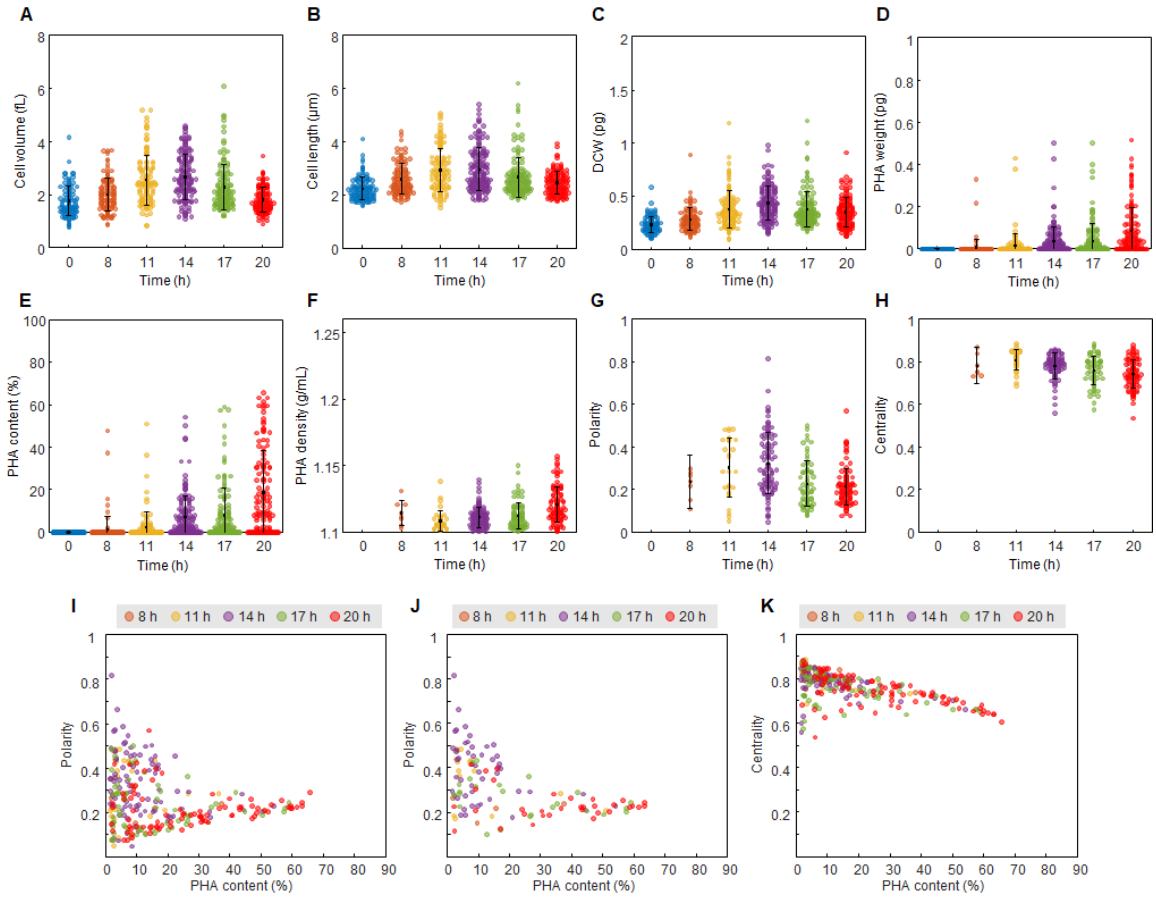

Fig. S12. ODT analyses for *P. putida* cells accumulating MCL-PHA. Quantification of (*A*) cell volume (fL), (*B*) cell length (μm), (*C*) DCW (pg), (*D*) PHA granule weight (pg), (*E*) PHA content (%, w/w), (*F*) PHA granule density (g/mL), (*G*) PHA granule polarity, and (*H*) PHA granule centrality of individual *P. putida* cells. (*I*, *J*) Scatter plots between polarity vs. PHA content for all cells analyzed and the cells longer than the average cell length, respectively. (*K*) Scatter plot between centrality vs. PHA content. The numbers of analyzed cells are 105, 109, 107, 152, 130, and 133 for 0, 8, 11, 14, 17, and 20 h, respectively. The bars indicate averages and standard deviations.

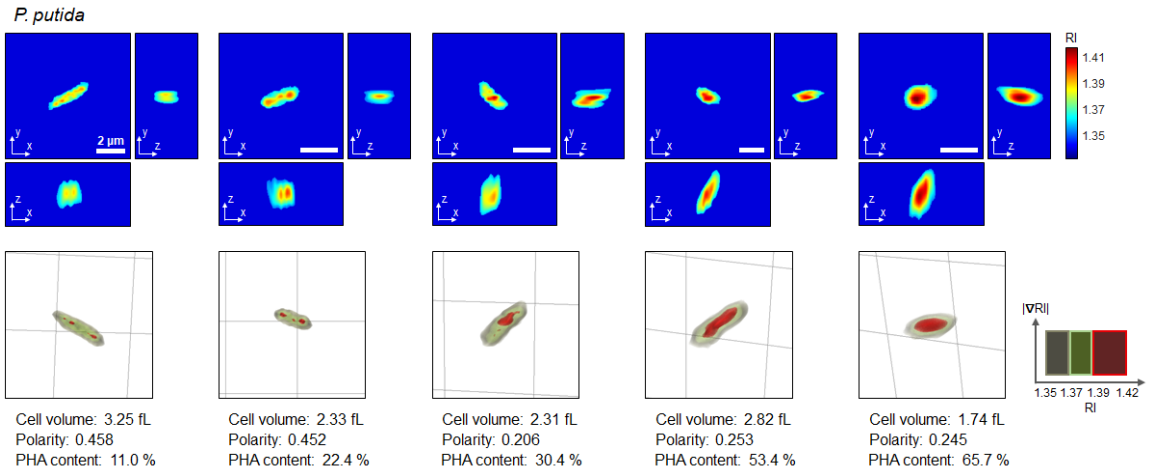

Fig. S13. Representative 3D RI distributions of *P. putida* cells. RI tomograms at selected x-y, y-z, and z-x planes (*Top*) and 3D rendering images (*Bottom*) of *P. putida* cells with different levels of PHA accumulation are shown. The quantified cell volume, polarity, and PHA content (%, w/w) are noted below the rendering images. One grid equals 5 μm.

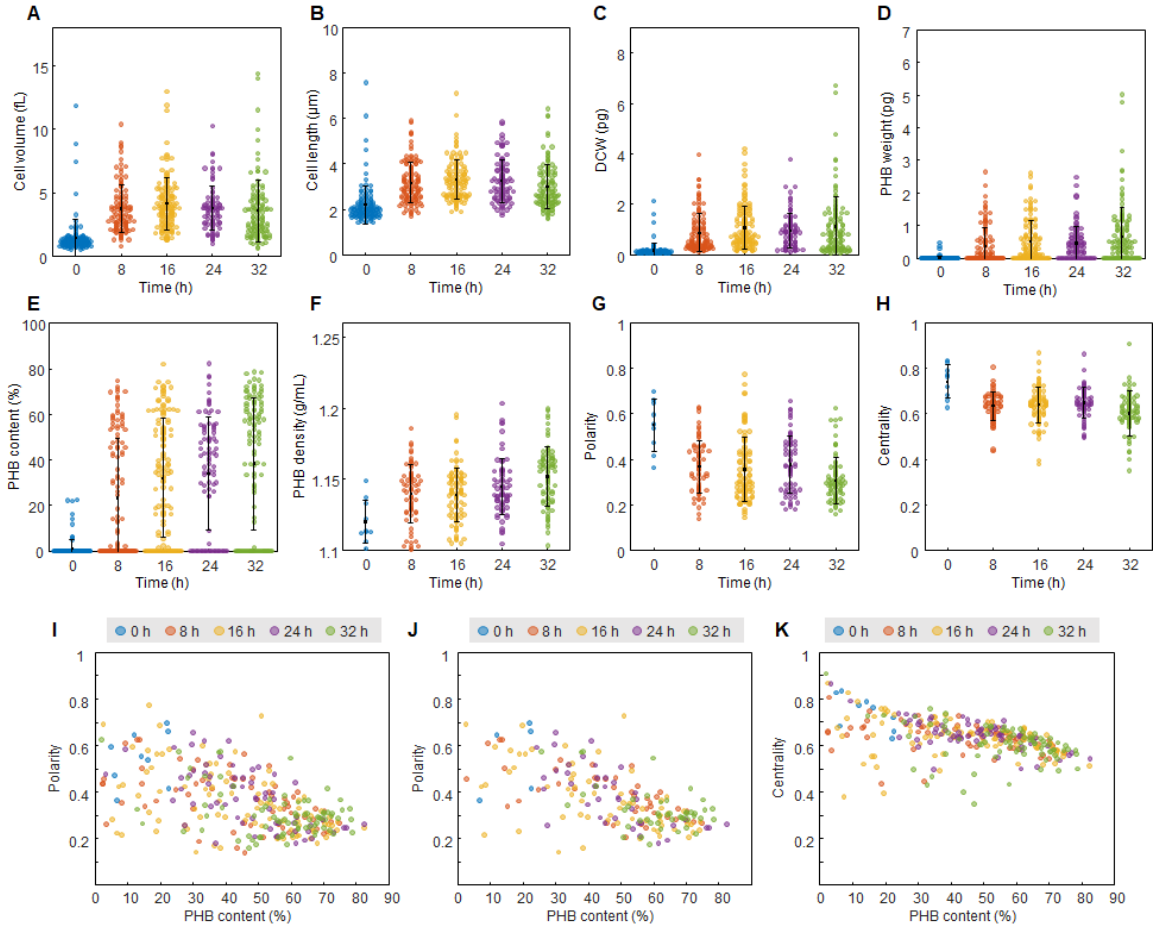

Fig. S14. ODT analyses for recombinant *K. pneumoniae* cells accumulating PHB. Quantification of (*A*) cell volume (fL), (*B*) cell length (μm), (*C*) DCW (pg), (*D*) PHB granule weight (pg), (*E*) PHB content (%, w/w), (*F*) PHB granule density (g/mL), (*G*) PHB granule polarity, and (*H*) PHB granule centrality of individual *K. pneumoniae* cells. (*I*, *J*) Scatter plots between polarity vs. PHB content for all cells analyzed and the cells longer than the average cell length, respectively. (*K*) Scatter plot between centrality vs. PHB content. The numbers of analyzed cells are 120, 120, 125, 93, and 123 for 0, 8, 16, 24 and 32 h, respectively. The bars indicate averages and standard deviations.

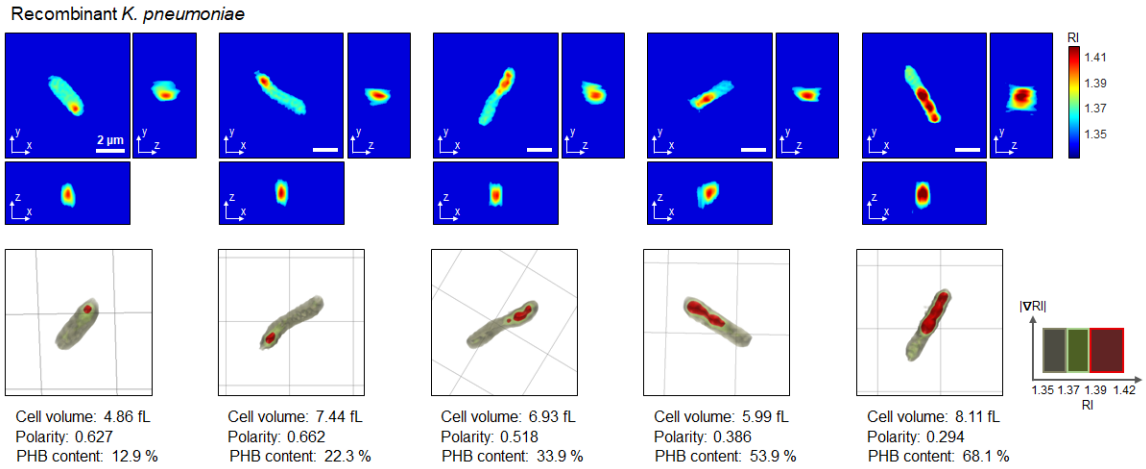

Fig. S15. Representative 3D RI distributions of recombinant *K. pneumoniae* cells. RI tomograms at selected x-y, y-z, and z-x planes (*Top*) and 3D rendering images (*Bottom*) of *K. pneumoniae* cells with different levels of PHB accumulation are shown. The quantified cell volume, polarity, and PHB content (%, w/w) are noted below the rendering images. One grid equals 5 μm.

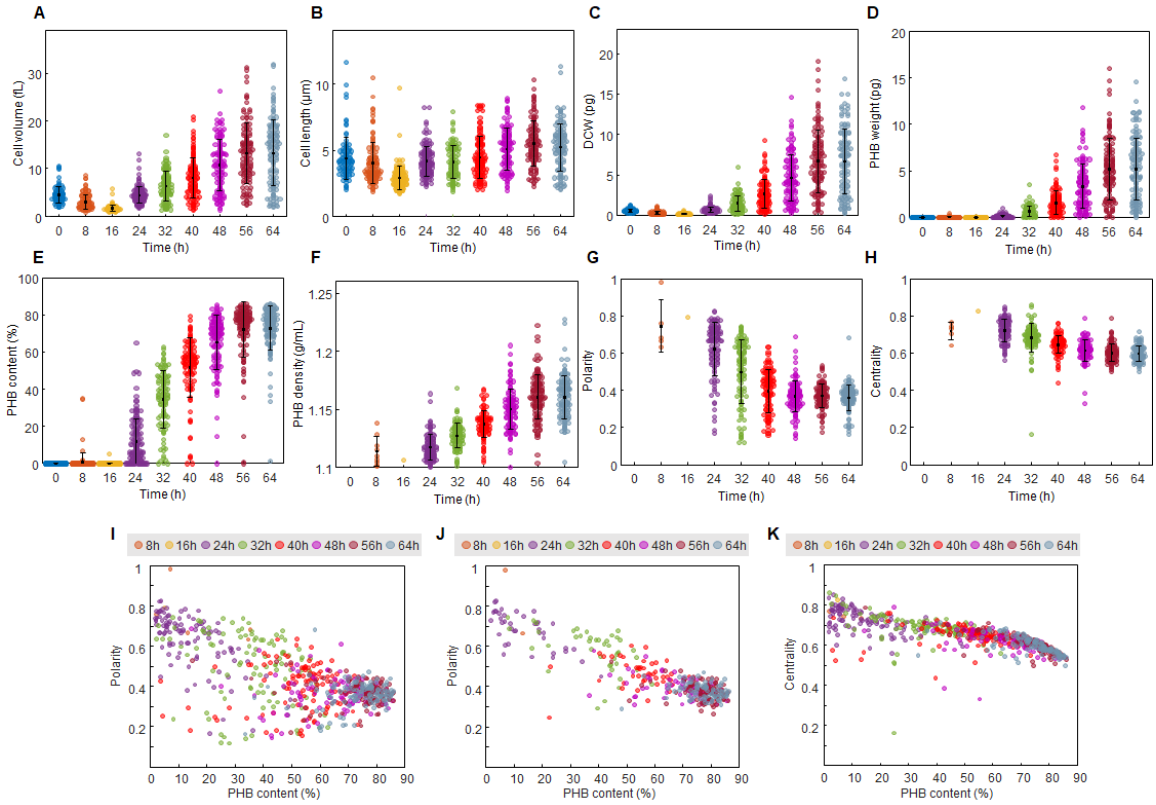

Fig. S16. ODT analyses for recombinant *E. coli* cells (expressing *C. necator phaP1*, *phaCAB*) accumulating PHB. Quantification of (*A*) cell volume (fL), (*B*) cell length (μm), (*C*) DCW (pg), (*D*) PHB granule weight (pg), (*E*) PHB content (%, w/w), (*F*) PHB granule density (g/mL), (*G*) PHB granule polarity, and (*H*) PHB granule centrality of individual recombinant *E. coli* cells. (*I*, *J*) Scatter plots between polarity vs. PHB content for all cells analyzed and the cells longer than the average cell length, respectively. (*K*) Scatter plot between centrality vs. PHB content. The numbers of analyzed cells are 93, 117, 119, 134, 111, 118, 115, 123, and 123 for 0, 8, 16, 24, 32, 40, 48, 56, and 64 h, respectively. The bars indicate averages and standard deviations.

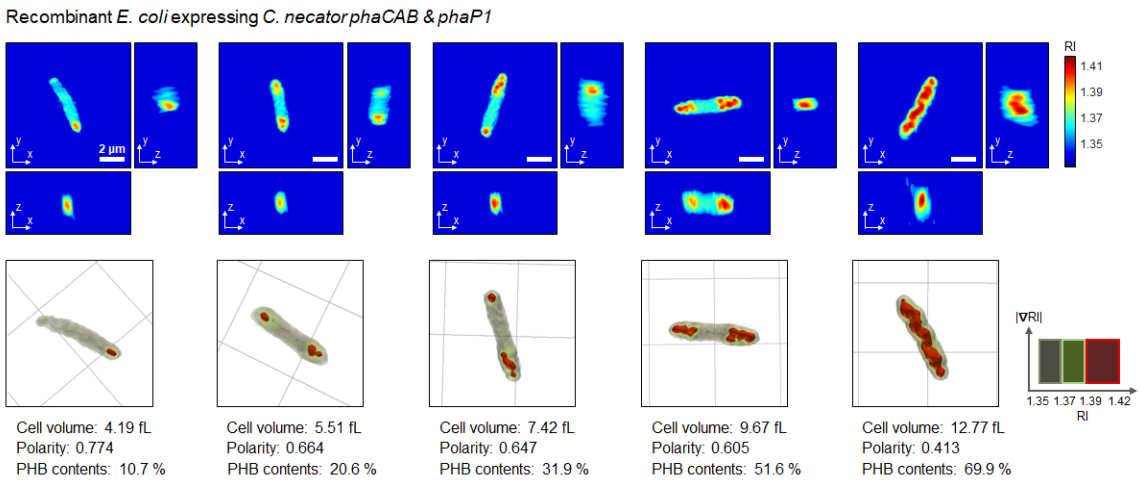

Fig. S17. Representative 3D RI distributions of recombinant *E. coli* (expressing *C. necator phaP1*, *phaCAB*) cells. RI tomograms at selected x-y, y-z, and z-x planes (*Top*) and 3D rendering images (*Bottom*) of the cells with different levels of PHB accumulation are shown. The quantified cell volume, polarity, and PHB content (%, w/w) are noted below the rendering images. One grid equals 5 μm.

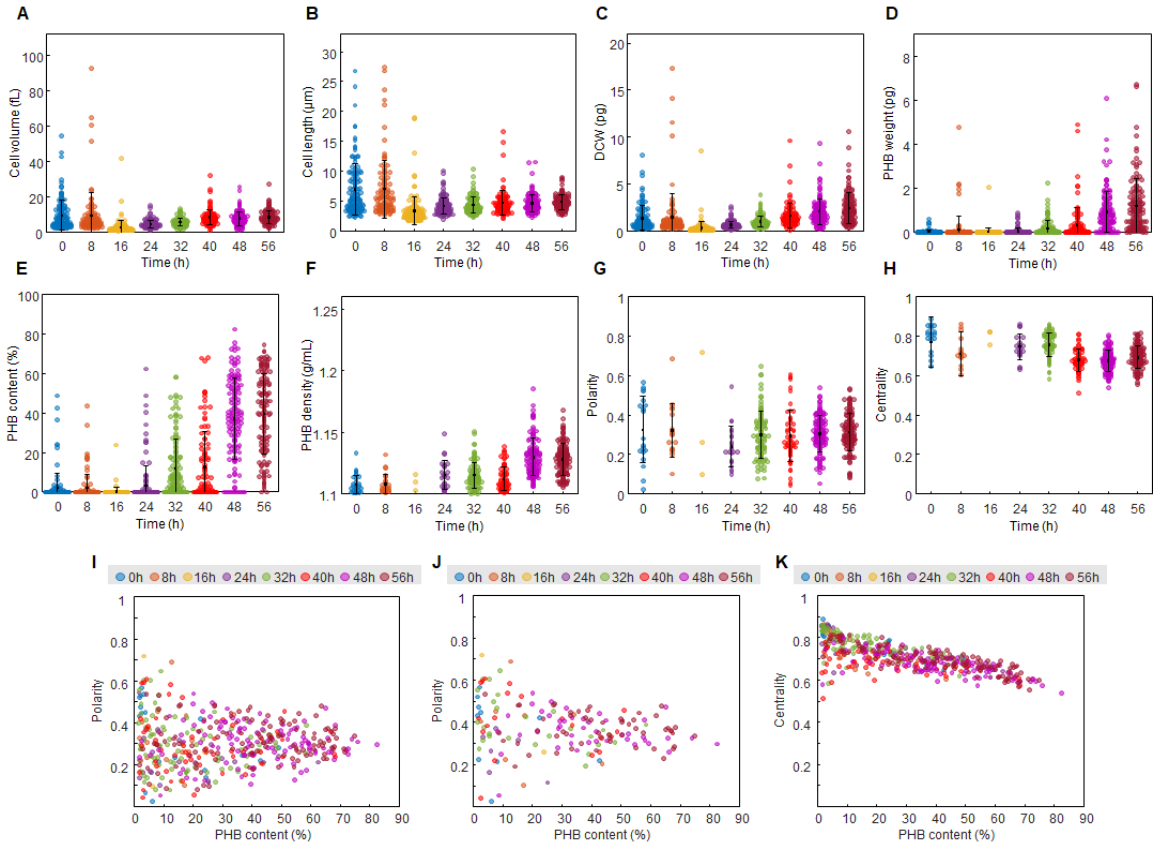

Fig. S18. ODT analyses for recombinant *E. coli* cells (expressing *C. necator phaM*, *phaCAB*) accumulating PHB. Quantification of (*A*) cell volume (fL), (*B*) cell length (μm), (*C*) DCW (pg), (*D*) PHB granule weight (pg), (*E*) PHB content (%, w/w), (*F*) PHB granule density (g/mL), (*G*) PHB granule polarity, and (*H*) PHB granule centrality of individual *E. coli* cells. (*I*, *J*) Scatter plots between polarity vs. PHB content for all cells analyzed and the cells longer than the average cell length, respectively. (*K*) Scatter plot between centrality vs. PHB content. The numbers of analyzed cells are 129, 104, 153, 135, 133, 104, 125, and 124 for 0, 8, 16, 24, 32, 40, 48, and 56 h, respectively. The bars indicate averages and standard deviations.

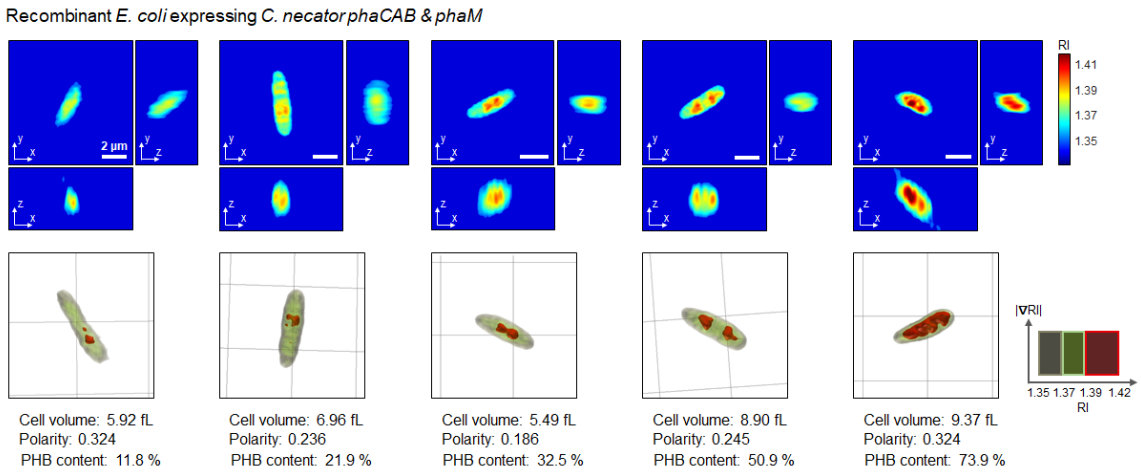

Fig. S19. Representative 3D RI distributions of recombinant *E. coli* (expressing *C. necator phaM*, *phaCAB*) cells. RI tomograms at selected x-y, y-z, and z-x planes (*Top*) and 3D rendering images (*Bottom*) of the cells with different levels of PHB accumulation are shown. The quantified cell volume, polarity, and PHB content (%, w/w) are noted below the 3D rendering images. One grid equals 5 μm.

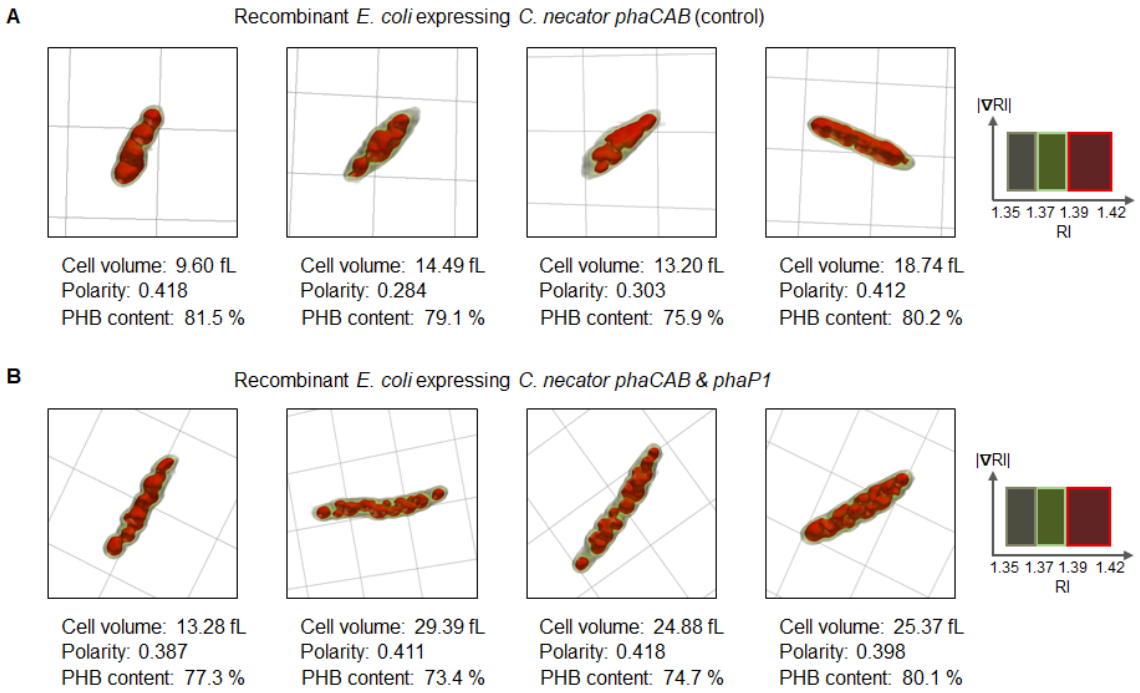

Fig. S20. 3D rendering images of recombinant *E. coli* cells. (*A*) *E. coli* expressing *C. necator phaCAB* genes. (*B*) *E. coli* expressing *C. necator phaCAB* and *phaP1* genes. This figure shows different morphologies of PHB granules between the two recombinant *E. coli* strains. The *phaP1*-expressing *E. coli* cells accumulated a larger number of PHB granules but each PHB granules were smaller in size. In the 3D rendering images, one grid equals 5 μm.

Table S1. Bacterial strains and plasmids used in this study.

Strain or plasmid	Description*	Reference
E. coli XL1-Blue	*E. coli recA1 endA1 gyrA96 thi-1 hsdR17 supE44 relA1 lac* [F′ *proAB lacI*^{q}*ZΔM15* Tn*10* (Tet^{R})]	Stratagene
C. necator	*C. necator* H16	Lab stock
P. putida	*P. putida* KT2440	Lab stock
K. pneumoniae	*K. pneumoniae* KCTC 2952	KCTC†
pCnCAB	pBluescript II KS(+) derivative; *C. necator* PHA biosynthesis operon promoter, *phaCAB* operon, transcriptional terminator of *C. necator* PHA biosynthesis operon, Ap^{R}	(1)
pPs619C1400Pct532-CnAB	pBluescript II KS(+) derivative; *C. necator* PHA biosynthesis operon promoter, *Pseudomonas* sp. MBEL 6-19 *phaC* variant (*phaC1400*; E130D, S325T, S477R, Q481M), *Clostridium propionicum pct* variant (*pct532*; A243T, silent mutation of A1200G), *C. necator phaAB*, transcriptional terminator of *C. necator* PHA biosynthesis operon, Ap^{R}	Lab stock
pCn-sfGFP-L-CAB	pCnCAB derivative; *C. necator* PHA biosynthesis operon promoter, *phaCAB* operon (*phaC* was replaced with *sfgfp*-linker-*phaC)*, transcriptional terminator of *C. necator* PHA biosynthesis operon, Ap^{R}	This study
pCn-sfGFP-CAB	pCnCAB derivative; *C. necator* PHA biosynthesis operon promoter, *sfgfp* gene, *phaCAB* operon, transcriptional terminator of *C. necator* PHA biosynthesis operon, Ap^{R}	This study
pCn-sfGFP-AB	pCnCAB derivative; *C. necator* PHA biosynthesis operon promoter, *phaCAB* operon (*phaC* was replaced with *sfgfp* gene), transcriptional terminator of *C. necator* PHA biosynthesis operon, Ap^{R}	This study
pKM312-cnCAB	Broad host range vector (pBBR1MCS) derivative, *tac* promoter*, C. necator phaCAB*, transcriptional terminator of *C. necator* PHA biosynthesis operon, Cm^{R}	This study
pCnP1CAB	pCnCAB derivative, *C. necator phaP1* was additionally introduced, Ap^{R}	This study
pCnMCAB	pCnCAB derivative, *C. necator phaM* was additionally introduced, Ap^{R}	This study

* Ap, ampicillin; Cm, chloramphenicol; R, resistance

† Korean Collection for Type Cultures, Daejeon, Republic of Korea

Table S2. PHA contents obtained by GC analysis.

Strain	PHA content (%, w/w)								
C. necator	0 h	8 h	16 h	24 h					
	n/a	55.0	69.1	79.7					
E. coli expressing *C. necator phaCAB*	0 h	8 h	16 h	24 h	32 h	40 h	48 h		
	n/a	n/a	39.0	65.3	78.2	83.3	91.9		
P. putida	0 h	8 h	11 h	14 h	17 h	20 h			
	n/a	27.9	35.6	38.6	29.4	31.8			
K. pneumoniae expressing *C. necator phaCAB*	0 h	8 h	16 h	24 h	32 h				
	n/a	24.1	33.7	45.9	40.5				
E. coli expressing *C. necator phaCAB, phaP1*	0 h	8 h	16 h	24 h	32 h	40 h	48 h	56 h	64 h
	n/a	n/a	5.8	50.4	66.7	78.6	85.1	86.5	89.5
E. coli expressing *C. necator phaCAB, phaM*	0h	8 h	16 h	24 h	32 h	40 h	48 h	56 h	
	n/a	n/a	36.3	26.8	53.2	72.1	76.9	81.4	

Movie S1 (separate file). Time-lapse movie of recombinant *E. coli* cells in a nutrient-rich medium for 240 minutes. The cells at the early period of cultivation (8 h) were analyzed. The 3D image was taken every 40 seconds. The brown, green, and red colors represent the RI region of 1.35–1.37, 1.37–1.39, and beyond 1.39 (corresponding to PHA granules), respectively.

Movie S2 (separate file). Time-lapse movie of *C. necator* cells in a nitrogen-limited medium for 200 minutes. The cells at 12 h of cultivation were analyzed. The 3D image was taken every 50 seconds. The brown, green, and red colors represent the RI region of 1.35–1.37, 1.37–1.39, and beyond 1.39 (corresponding to PHA granules), respectively.

Movie S3 (separate file). Time-lapse movie of *C. necator* cells in a nutrient-rich medium for 174 minutes. The cells at 12 h of cultivation were analyzed. The 3D image was taken every two minutes. The brown, green, and red colors represent the RI region of 1.35–1.37, 1.37–1.39, and beyond 1.39 (corresponding to PHA granules), respectively.

Movie S4 (separate file). Time-lapse movie of recombinant *E. coli* cells in a nutrient-rich medium for 520 minutes. The cells at 20 h of cultivation were analyzed. The 3D image was taken every ten minutes. The brown, green, and red colors represent the RI region of 1.35–1.37, 1.37–1.39, and beyond 1.39 (corresponding to PHA granules), respectively.

Movie S5 (separate file). Time-lapse movie of *P. putida* cells in a nitrogen-limited medium for 120 minutes. The cells at 12 h of cultivation were analyzed. The 3D image was taken every 50 seconds. The brown, green, and red colors represent the RI region of 1.35–1.37, 1.37–1.39, and beyond 1.39 (corresponding to PHA granules), respectively.

Movie S6 (separate file). Time-lapse movie of recombinant *K. pneumoniae* cells in a nitrogen-rich medium for 182 minutes. The cells at 12 h of cultivation were analyzed. The 3D image was taken every 20 seconds. The brown, green, and red colors represent the RI region of 1.35–1.37, 1.37–1.39, and beyond 1.39 (corresponding to PHA granules), respectively.

SI References

1. T. H. Yang *et al*., Biosynthesis of polylactic acid and its copolymers using evolved propionate CoA transferase and PHA synthase. *Biotechnol. Bioeng.* **105**, 150–160 (2010).
2. S. Y. Choi, I. J. Cho, Y. Lee, S. Park, S. Y. Lee, Biocatalytic synthesis of polylactate and its copolymers by engineered microorganisms. *Methods Enzymol.* **627**, 125–162 (2019).
3. G. Braunegg, B. Y. Sonnleitner, R. M. Lafferty, A rapid gas chromatographic method for the determination of poly-β-hydroxybutyric acid in microbial biomass. *Appl. Microbiol. Biotechnol.* **6**, 29–37 (1978).
4. Y. K. Jung, T. Y. Kim, S. J. Park, S. Y. Lee, Metabolic engineering of *Escherichia coli* for the production of polylactic acid and its copolymers. *Biotechnol. Bioeng.* **105**, 161–171 (2010).
5. G. Popescu, Quantitative phase imaging of cells and tissues, (McGraw Hill Professional, 2011).
6. K. Lee *et al*., Quantitative phase imaging techniques for the study of cell pathophysiology: from principles to applications. *Sensors* **13**, 4170–4191 (2013).
7. M. Takeda, H. Ina, S. Kobayashi, Fourier-transform method of fringe-pattern analysis for computer-based topography and interferometry. *J. Opt. Soc. Am.* **72**, 156–160 (1982).
8. S. K. Debnath, Y. Park, Real-time quantitative phase imaging with a spatial phase-shifting algorithm. *Opt. Lett.* **36**, 4677–4679 (2011).
9. E. Wolf, Three-dimensional structure determination of semi-transparent objects from holographic data. *Opt. Commun.* **1**, 153–156 (1969).
10. K. Kim *et al*., High-resolution three-dimensional imaging of red blood cells parasitized by *Plasmodium falciparum* and in situ hemozoin crystals using optical diffraction tomography. *J. Biomed. Opt.* **19**, 011005 (2013).

11. J. Lim *et al*., Comparative study of iterative reconstruction algorithms for missing cone problems in optical diffraction tomography. *Opt. Express* **23**, 16933–16948 (2015).
12. S. Shin, K. Kim, J. Yoon, Y. Park, Active illumination using a digital micromirror device for quantitative phase imaging. *Opt. Lett.* **40**, 5407–5410 (2015).
13. K. Lee, K. Kim, G. Kim, S. Shin, Y. Park, Time-multiplexed structured illumination using a DMD for optical diffraction tomography. *Opt. Lett.* **42**, 999–1002 (2017).
14. G. Choi *et al*., Cycle-consistent deep learning approach to coherent noise reduction in optical diffraction tomography. *Opt. Express* **27**, 4927–4943 (2019).
15. E. A. Dawes, P. J. Senior, "The Role and Regulation of Energy Reserve Polymers in Micro-organisms" in Advances in Microbial Physiology Vol. 10, A. H. Rose, D. W. Tempest, Eds. (Academic Press, 1973), pp. 135–266.
16. S. Maj, On the relationship between refractive index and density for SiO_2 polymorphs. *Phys. Chem. Miner.* **10**, 133–136 (1984).
17. H. N. Ritland, Density phenomena in the transformation range of a borosilicate crown glass. *J. Am. Ceram. Soc.* **37**, 370–377 (1954).
18. R. Barer, Determination of dry mass, thickness, solid and water concentration in living cells. *Nature* **172**, 1097–1098 (1953).
19. R. Barer, S. Joseph, Refractometry of living cells. *J. Cell Sci.* **95**, 399–423 (1954).
20. C. Di Primo, I. Lebars, Determination of refractive index increment ratios for protein–nucleic acid complexes by surface plasmon resonance. *Anal. Biochem.* **368**, 148–155 (2007).
21. C.-Y. Tan, Y.-X. Huang, Dependence of Refractive Index on Concentration and Temperature in Electrolyte Solution, Polar Solution, Nonpolar Solution, and Protein Solution. *J. Chem. Eng. Data* **60**, 2827–2833 (2015).
22. W.M.b.M. Yunus, A.b.A. Rahman, Refractive index of solutions at high concentrations. *Appl. Opt.* **27**, 3341–3343 (1988).
23. J. Jung *et al*., Label-free non-invasive quantitative measurement of lipid contents in individual microalgal cells using refractive index tomography. *Sci. Rep.* **8**, 6524 (2018).
24. V. Peters, B. H. Rehm, In vivo monitoring of PHA granule formation using GFP-labeled PHA synthases. *FEMS Microbiol. Lett.* **248**, 93–100 (2005).
25. F. Mravec *et al*., Accumulation of PHA granules in *Cupriavidus necator* as seen by confocal fluorescence microscopy. *FEMS Microbiol. Lett.* **363**, fnw094 (2016).
26. D. Jendrossek, Fluorescence microscopical investigation of poly (3-hydroxybutyrate) granule formation in bacteria. *Biomacromolecules* **6**, 598–603 (2005).
27. J. Tian, A. J. Sinskey, J. Stubbe, Kinetic studies of polyhydroxybutyrate granule formation in *Wautersia eutropha* H16 by transmission electron microscopy. *J. Bacteriol.* **187**, 3814–3824 (2005).
28. A. Wahl, N. Schuth, D. Pfeiffer, S. Nussberger, D. Jendrossek, PHB granules are attached to the nucleoid via PhaM in *Ralstonia eutropha*. *BMC Microbiol.* **12**, 262 (2012).
29. M. Beeby, M. Cho, J. Stubbe, G. J. Jensen, Growth and localization of polyhydroxybutyrate granules in *Ralstonia eutropha*. *J. Bacteriol.* **194**, 1092–1099 (2012).
30. Y. Kim, J. Jeong, J. Jang, M. W. Kim, Y. Park, Polarization holographic microscopy for extracting spatio-temporally resolved Jones matrix. *Opt. Express* **20**, 9948–9955 (2012).
31. J. Jung, K. Kim, J. Yoon, Y. Park, Hyperspectral optical diffraction tomography. *Opt. Express* **24**, 2006–2012 (2016).